Supporting Information

Axial Chlorine Coordination Reconstructs Fe–N_4 Electronic Structure for Efficient pH-Universal Oxygen Reduction Reaction

Yanle Yuan[1†], Xia Zhang[2†], Feilong Qin[1], Chunwu Lei[1], Yang Wang[1], Yaoyu Yang[1], Guang Feng[3], Kaiyu Liu[1]* and Tao Chen[1]**

[1] College of Chemistry and Chemical Engineering, Hunan Provincial Key Laboratory of Chemical Power Sources, Central South University, Changsha 410083, China

[2] Helmholtz-Zentrum Berlin für Materialien und Energie GmbH, Hahn-Meitner-Platz 1, 14109 Berlin Germany

[3] Beijing Key Laboratory for Chemical Power Source and Green Catalysis, School of Chemistry and Chemical Engineering, Beijing Institute of Technology, Beijing, 100811 China

† Y. Y. and Z.X. contributed equally to the work.

* E-mail: taochen4486@163.com (T. Chen); kaiyuliu309@163.com (K. Liu); fg@bit.edu.cn (G, Feng)

Table of Contents

Section S1. Experimental Procedure

1.1 Experimental methods

Materials: $Zn(NO_3)_2 \cdot 6H_2O$, $Fe(NO_3)_3 \cdot 9H_2O$, KOH and 2-Methylimidazole were purchased from Sinopharm Chemical Reagent Co. 20 wt% Pt/C, 5% Nafion and RuO_2 were purchased from Sigma-Aldrich. All reagents are in analytical level.

Synthesis of ZIF-8@Fe_x: Dissolve 10 mmol of $Zn(NO_3)_2 \cdot 6H_2O$, x mmol of $Fe(NO_3)_3 \cdot 9H_2O$ (x = 0, 0.05, 0.1, 0.2, 0.5 mmol), and 80 mmol of 2-methylimidazole separately in 30 mL of methanol, and stir for 10 minutes. After all solids are completely dissolved, mix the solutions and initiate stirring. After five minutes, the mixture appears slightly milky. Stir the solution at room temperature for 24 hours. Collect the precipitated product by centrifugation and wash it three times with methanol. Dry the obtained solid under vacuum at 60°C for 24 hours to obtain ZIF-8@Fe_x powder.

Synthesis of Zk-Fe_x-ClNC: Physically mix ZIF-8@Fe_x and NaCl at a mass ratio of 1:1. The resulting mixture is heated under a flowing Ar atmosphere at a heating rate of $5°C \cdot min^{-1}$ to 950°C and maintained for 2 hours. After obtaining the black powder sample, wash it with deionized water for 24 hours, filter, and dry under vacuum at 80°C for 24 hours to collect the product as Zk-Fe_x-ClNC (x = 0, 0.05, 0.1, 0.2, 0.5).

Synthesis of Z-$Fe_{0.1}$-NC: The preparation method is the same as in section 4.2.3, except that no NaCl is added during calcination.

Aqueous Zn-air batteries: Zn-air batteries mainly consist of cathode, anode and electrolyte. The anode is made of polished zinc flakes, the electrolytes are 6 M KOH and 6 M KOH+0.2 M $(CH_3COO)_2Zn$. The cathode was composed of carbon paper, nickel foam and waterproof breathable membrane in order from inside to outside, and the uniformly dispersed catalyst material was dropped on the carbon paper as the cathode reaction catalyst with a loading of 1 mg cm^{-2}.

1.2 Characterizations

Characterizations. X-ray diffraction (XRD) tests were carried out by D8Advance diffractometer with a radiation source of Cu Kα (λ=0.15406 nm), $10° \leq 2\theta \leq 80°$, 10°/min.

Scanning electron microscope (SEM) images were acquired by TESCAN MIRA LMS. Transmission electron microscopy (TEM) images were obtained by FEI Talos F200S transmission electron microscope with the test material currently dispersed ultrasonically in ethanol. X-ray photoelectron spectroscopy (XPS)was measured using Thermo Scientific ESCALAB250Xi spectrometer with an Al Kα radiation source, and all binding energy values were calibrated against C 1s (284.8 eV). Raman spectra was collected by Renishaw Raman Spectrometer (λ=532 nm). The isothermal adsorption-desorption curves for low-temperature nitrogen were measured on an ASAP-2460, the Brunauer-Emmett-Teller (BET) model was chosen for the calculation of the specific surface area, and the Barrett-Joyner-Halenda (BJH) model was used to obtain the pore size distribution data. The Fe K-edge spectra were collected in fluorescence mode at beamline 1W2B with a Si (111) double-crystal monochromator at the Synchrotron Radiation Facility, Helmholtz Zentrum Berlin, Berlin, Germany. The ATHENA software package was used to analyze the XANES and EXAFS data.

1.3 Electrochemical measurement

Electrochemical Measurements. The electrochemical performance tests were carried out using CHI 760E workstation and standard three-electrode test system. The catalyst ink was obtained with the following method: 2 mg of catalyst was scattered in 480 μL of ethanol and ultrasonicated for 30 minutes, and then ultrasonicated again after the addition of Nafion (20 μL, 5wt%). Then 10 μL of catalyst ink was dropwise placed on the glassy carbon electrode and dried at natural to obtain the working electrode. All initially recorded potentials were then normalized to the reversible hydrogen electrode (RHE) in accordance with the Nernst formula:

$$E_{RHE} = E_{Hg/Hg_2Cl_2} + 0.0592 * pH + 0.242V \quad (1\text{-}1)$$

$$E_{RHE} = E_{Ag/AgCl} + 0.0592 * pH + 0.197V \quad (1\text{-}2)$$

$$E_{RHE} = E_{Hg/HgO} + 0.0592 * pH + 0.098V \quad (1\text{-}3)$$

Koutecky-Levich (K-L) plots were employed for the calculation of electron transfer number (n):

$$\frac{1}{J}=\frac{1}{J_L}+\frac{1}{J_K}=\frac{1}{B\omega^{1/2}}+\frac{1}{J_K} \quad (1\text{-}4)$$

$$B=0.62nFC_0D_0^{2/3}\nu^{-1/6} \quad (1\text{-}5)$$

F=96485 C mol^{-1}, C_0=1.2x10^{-6} mol cm^{-3}, D_0=1.9x10^{-5} cm^2 s^{-1} and ν=0.01 cm^2 s^{-1}.

The rotating disk ring experiment (RRDE) ring electrode was set at 1.2 V and the ring electrode collection efficiency was 0.37. Hydrogen peroxide H_2O_2 yields and the electron transfer number (n) during the ORR process were calculated by the following equations:

$$\%H_2O_2=200\frac{I_R/N}{I_D+I_R/N} \quad (1\text{-}6)$$

$$n=\frac{I_D}{I_D+I_R/N} \quad (1\text{-}7)$$

Section S2. Density function theory calculations

Density function theory calculations: The calculations were performed using the Vienna Ab initio Simulation Package (VASP) with the Projector Augmented Wave (PAW) method. Density functional theory (DFT) calculations were carried out within a plane-wave basis set under periodic boundary conditions, with a plane-wave cut-off energy of 450 eV. The Perdew-Burke-Ernzerhof (PBE) exchange-correlation functional and the van der Waals density functional (vdW-DF) were employed within the generalized gradient approximation (GGA). The Brillouin zone was sampled using a 3×3×1 k-point grid within the Monkhorst-Pack scheme. The convergence criteria for the total energy and interatomic forces were set to 10^{-5} eV per unit cell and 0.01 eV·Å^{-1}, respectively. A vacuum layer of 15 Å was applied above the top layer to avoid interactions between periodic images. The free energies of oxygen reduction reaction (ORR) intermediates were obtained by incorporating entropy, zero-point energy, and enthalpy corrections based on statistical thermodynamics for all adsorbed species. The corresponding values for gas-phase molecules were taken from the standard NIST-JANAF thermochemical tables. The reaction energies for the overall ORR process were calculated according to the method developed by Nørskov et al.

The simulation method of the four-electron ORR pathway is as follows :

$$O_2+*\rightarrow *OO$$

$$*OO+H_2O+e^-\rightarrow *OOH+OH^-$$

$$*OOH+e^-\rightarrow *O+OH^-$$

$$*O+ H_2O+e^-\rightarrow *OH+OH^-$$

$$*OH+e^-\rightarrow *+OH^-$$

Section S3. Supplementary Figures and Tables

3.1 Supplemental Figures

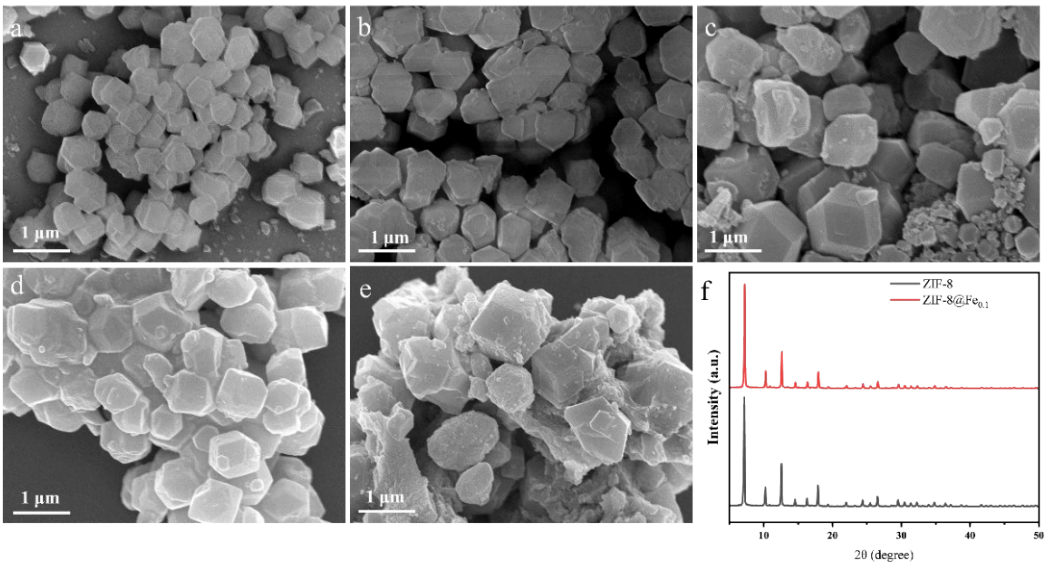

Figure S1. (a-e)SEM images of IF-8@Fe_0，ZIF-8@$Fe_{0.02}$，ZIF-8@$Fe_{0.1}$，ZIF-8@$Fe_{0.2}$，ZIF-8@$Fe_{0.5}$ and (f) XRD pattern of ZIF-8@Fe_0 和 ZIF-8@$Fe_{0.1}$

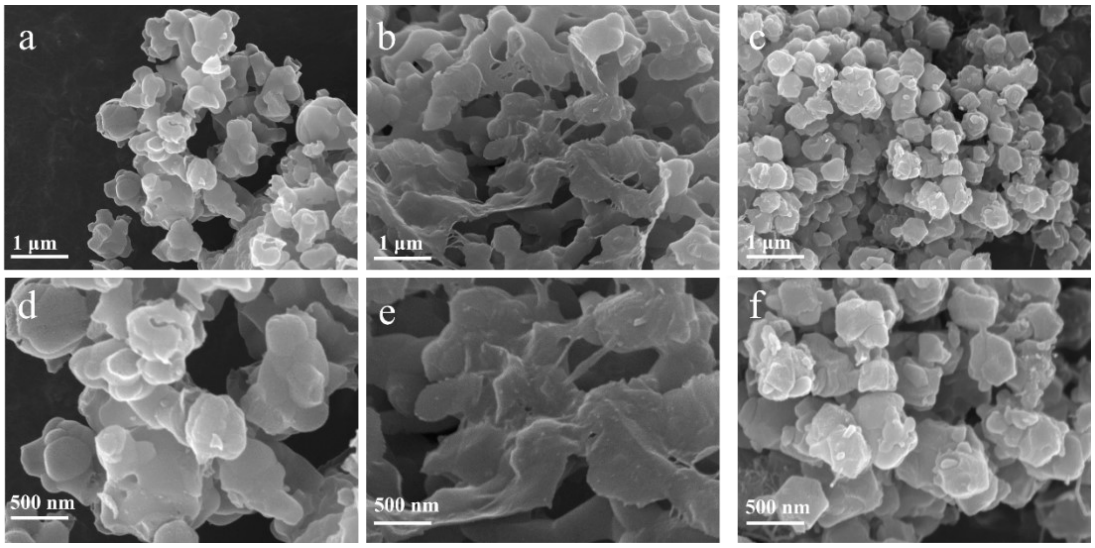

Figure S2. SEM patterns of Zk-Fe_0-ClNC (a, d), Zk-$Fe_{0.1}$-ClNC (b, e) and Z-Fe_0-NC (e, f)

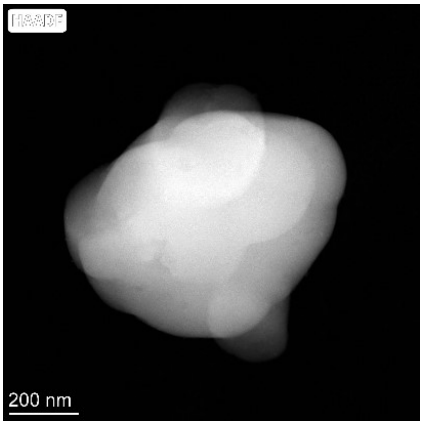

Figure S3. HAADF-TEM image of Zk-$Fe_{0.1}$-ClNC

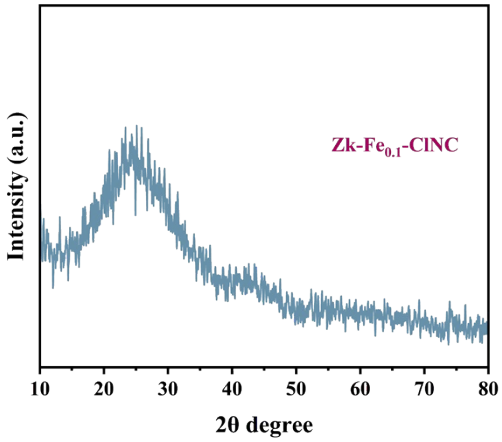

Figure S4. XRD image of Zk-$Fe_{0.1}$-ClNC

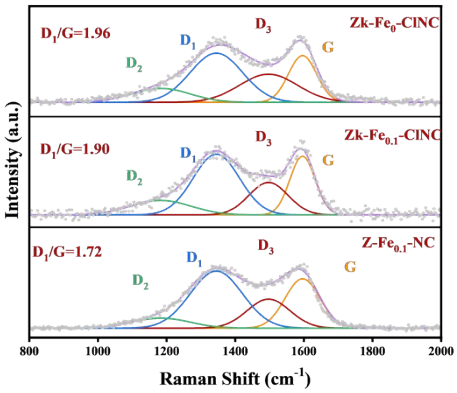

Figure S5. Raman of Zk-Fe_0-ClNC, Zk-$Fe_{0.1}$-ClNC and Z-$Fe_{0.1}$-NC

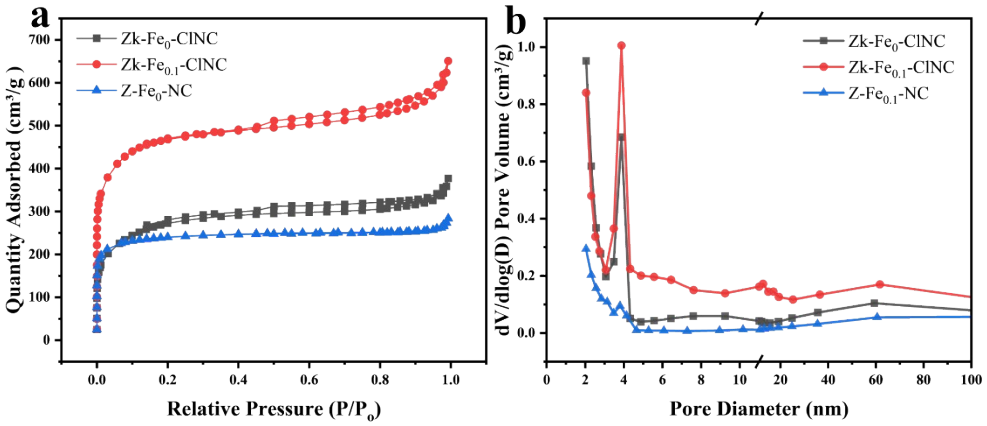

Figure S6. N_2 gas adsorption and desorption curves and (b) Pore size distribution of Zk-Fe_0-ClNC, Zk-$Fe_{0.1}$-ClNC and Z-$Fe_{0.1}$-NC samples

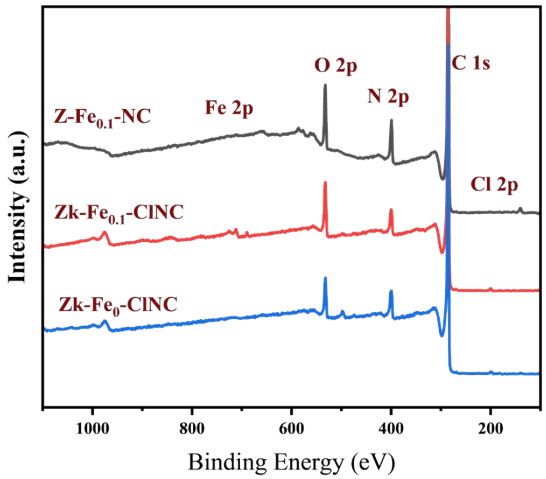

Figure S7. XPS full spectra of Zk-Fe_0-ClNC, Zk-$Fe_{0.1}$-ClNC and Z-$Fe_{0.1}$-NC samples

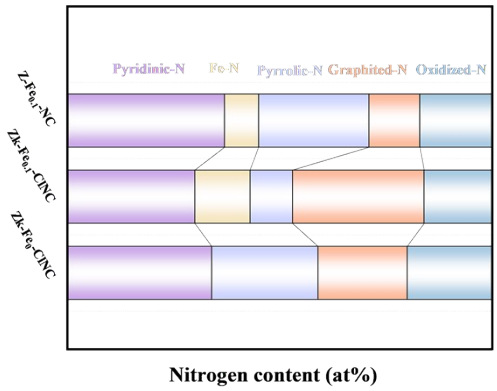

Figure S8. scaled plots of various nitrogen contents

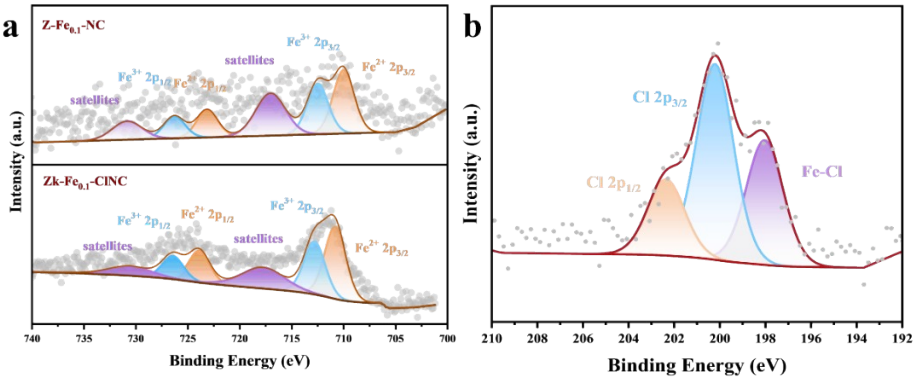

Figure S9. (a) Fe XPS spectra of Zk-$Fe_{0.1}$-ClNC and Z-$Fe_{0.1}$-NC samples, (b) Cl XPS spectra of Zk-$Fe_{0.1}$-ClNC

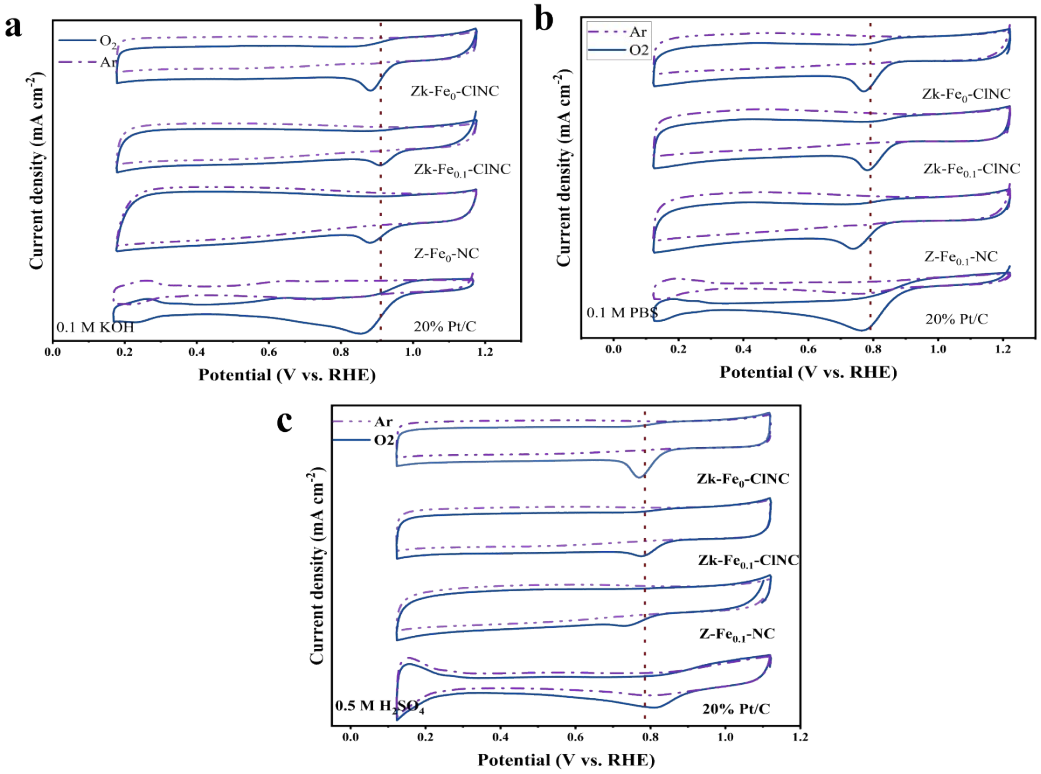

Figure S10. CV curve of various catalysts in different electrolytes: (a) 0.1 M KOH (b) 0.1 M PBS (c) 0.5 M H_2SO_4

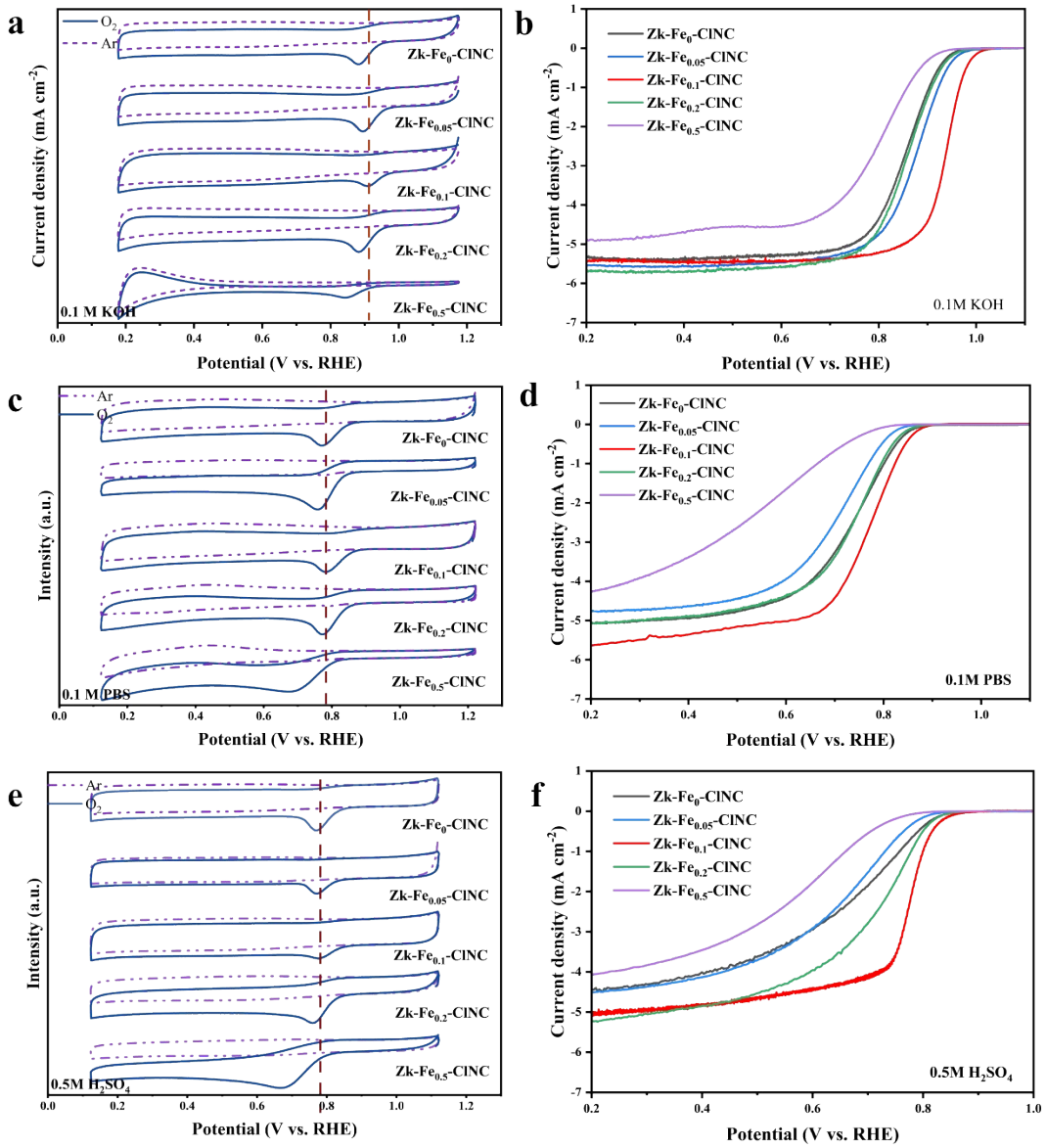

Figure S11. Electrochemical catalytic activity of Zk-Fe$_x$-ClNC (x=0, 0.05, 0.1, 0.2, 0.5 mmol) in different electrolytes: 0.1 M KOH (a) CV test and (b) LSV test; 0.1 M PBS (a) CV test and (b) LSV test; 0.5 M H_2SO_4 (a) CV test and (b) LSV test.

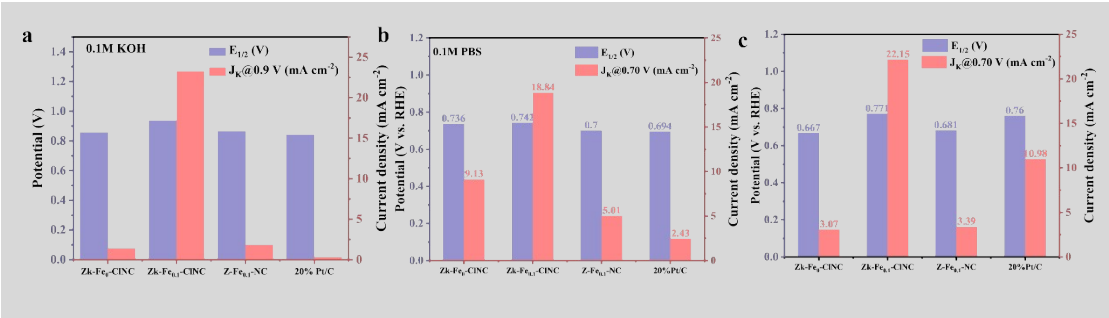

Figure S12. Tafel plots and comparison of $E_{1/2}$ and J_k in different electrolytes: （a）0.1M KOH （b）0.1M PBS and（c）0.5M H_2SO_4

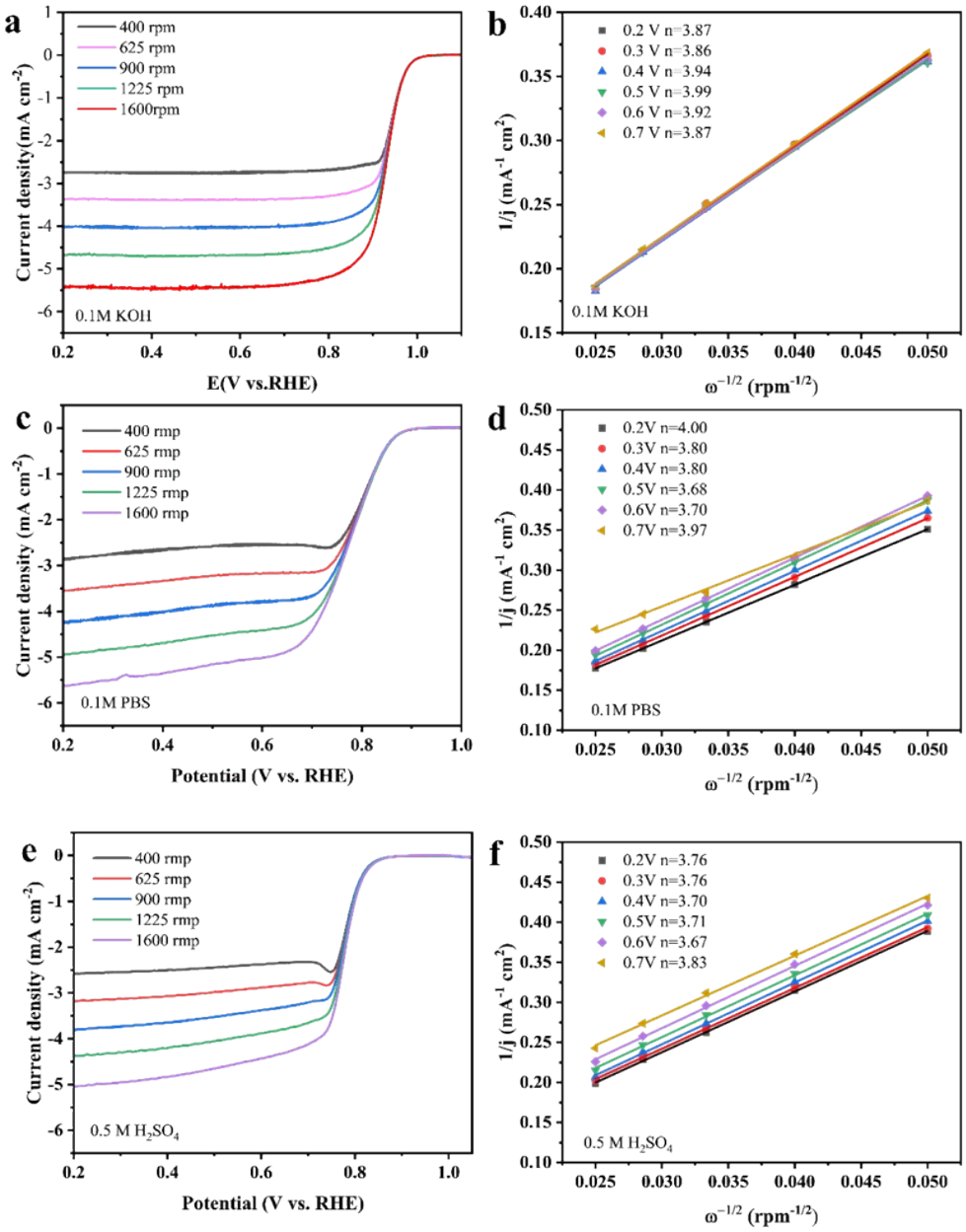

Figure S13. LSV curves and (b) K-L fitted curves of Zk-$Fe_{0.1}$-ClNC catalysts at 0.1 M KOH (a) different rotational speeds, 0.1 M PBS (a) different rotational speeds, and (b) K-L fitted curves of 0.5 M H_2SO_4 (a) different rotational speeds

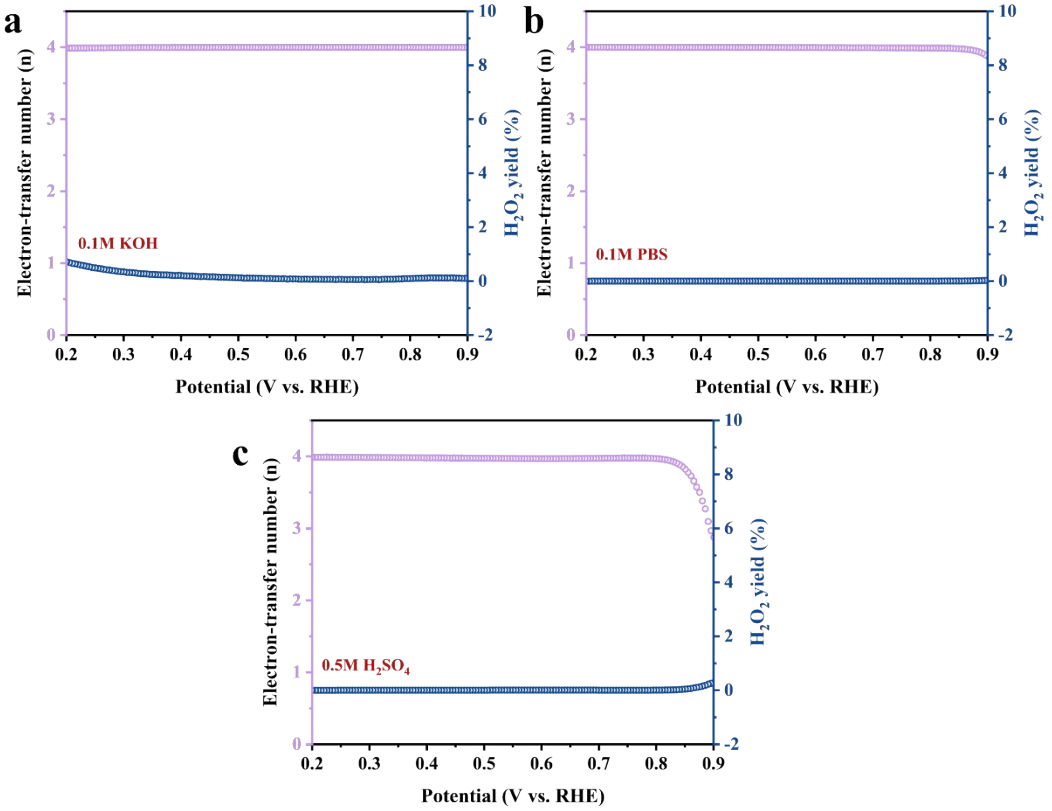

Figure S14. Electron transfer number (***n***) and hydrogen peroxide yield (%) of Zk-$Fe_{0.1}$-ClNC catalyst in different electrolytes: (a) 0.1 M KOH (b) 0.1 M PBS and (c) 0.5 M H_2SO_4.

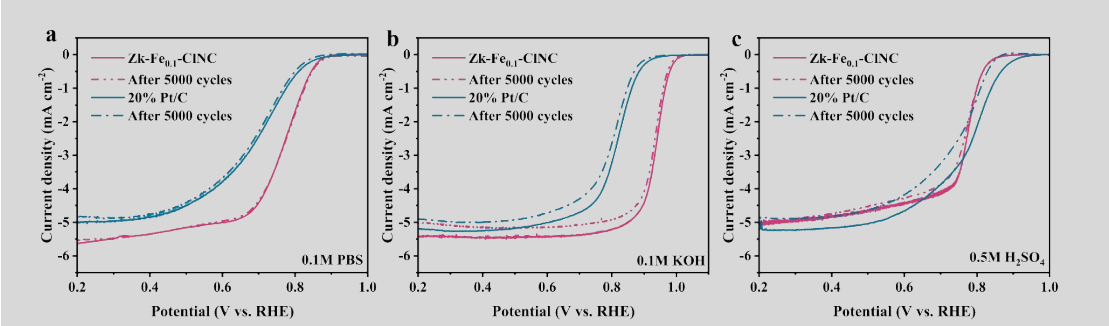

Figure S15. cyclic durability test in different electrolytes: （a）0.1M KOH （b）0.1M PBS and（c）0.5M H_2SO_4

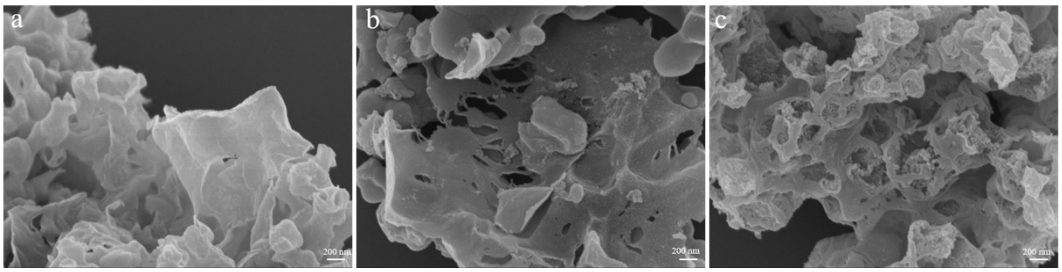

Figure S16. SEM images of the Zk-$Fe_{0.1}$-ClNC catalyst after cycling in different electrolytes: （a）0.1M KOH （b）0.1M PBS and（c）0.5M H_2SO_4

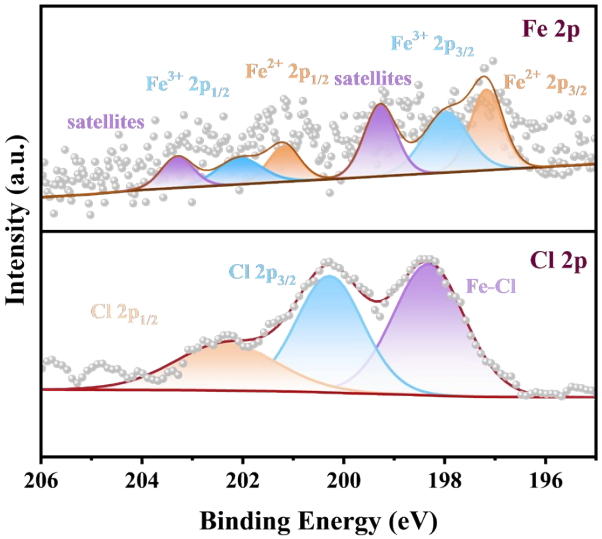

Figure S17. (a) Fe XPS spectra and Cl XPS spectra of Zk-$Fe_{0.1}$-ClNC catalyst after cycling in 0.5M H_2SO_4 electrolytes.

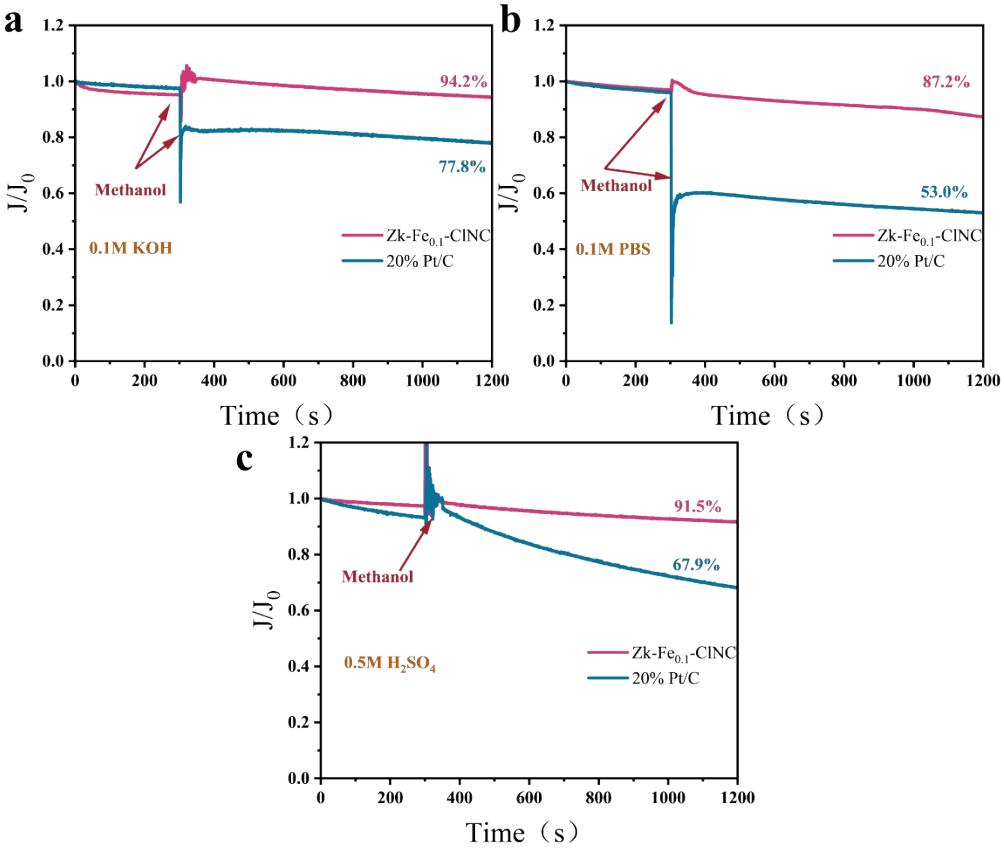

Figure S18. methanol resistance test

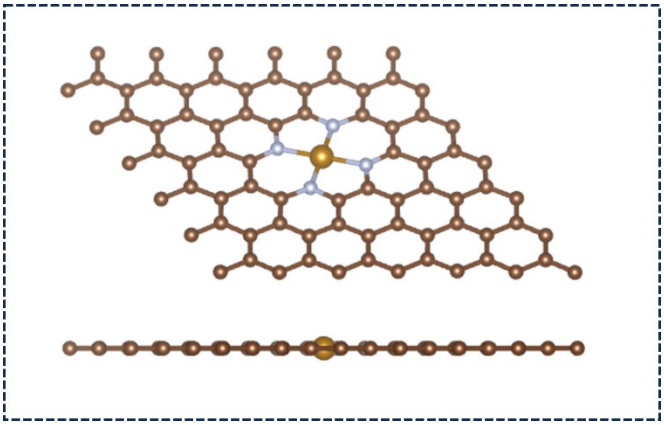

Figure S19. The model structure of Fe-N_4-C.

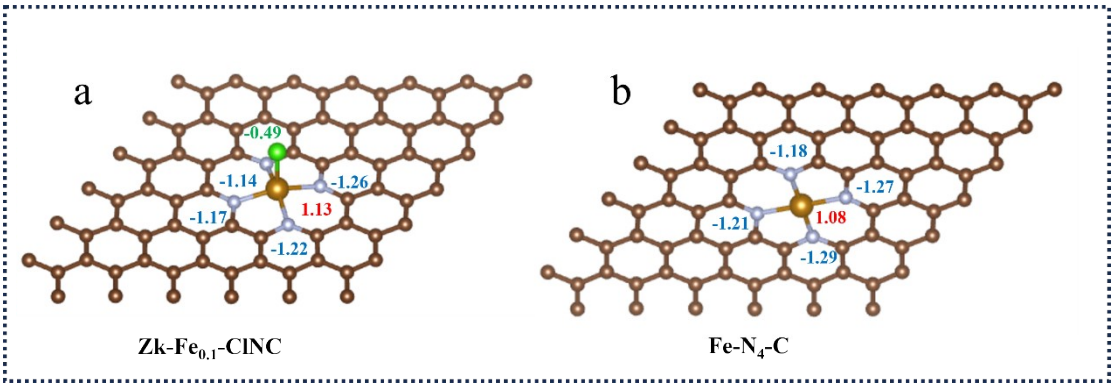

Figure S20. Schematic diagram of Bader charge analysis for Zk-$Fe_{0.1}$-ClNC (a) and Fe-N_4-C (b).

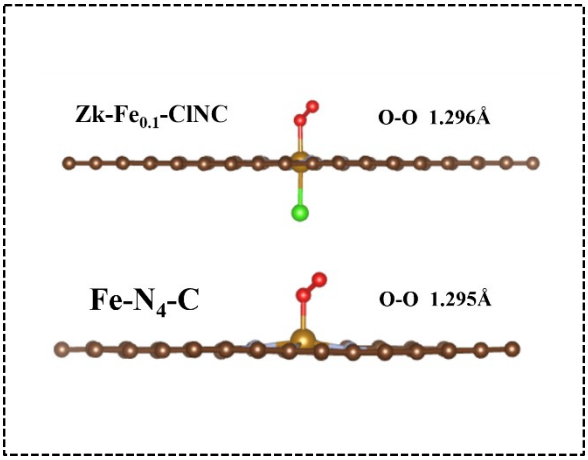

Figure S21. O_2 adsorption model for Zk-$Fe_{0.1}$-ClNC and Fe-N_4-C.

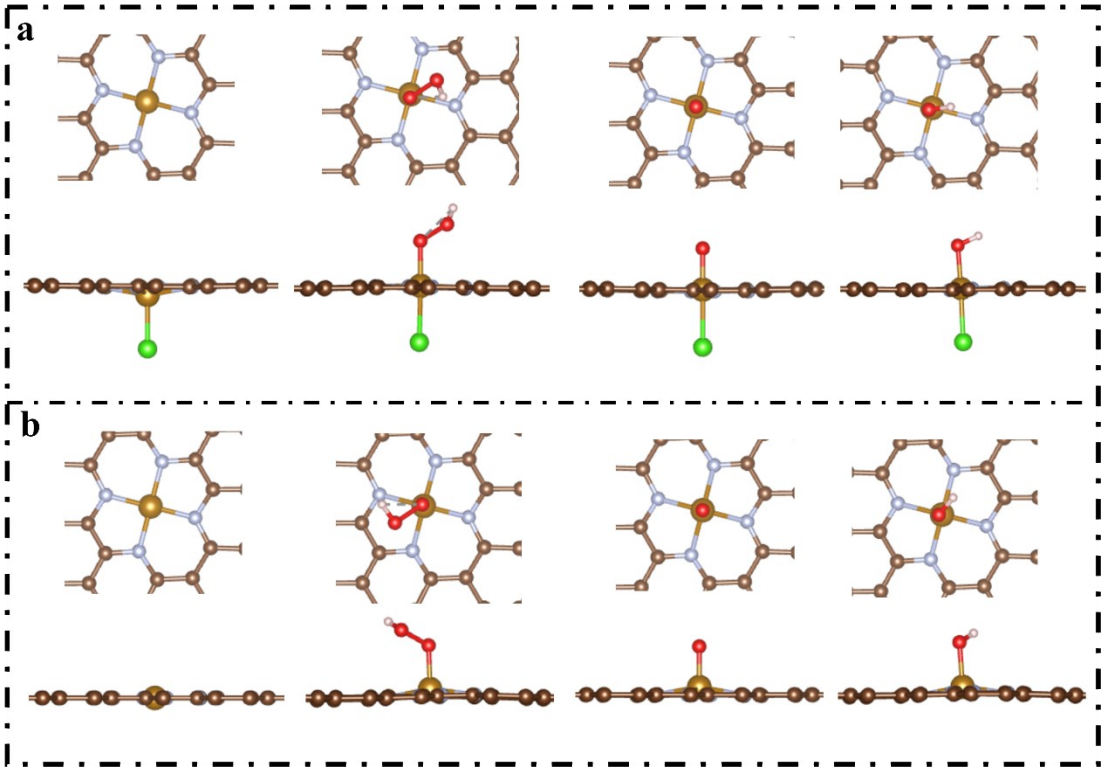

Figure S22. ORR reaction intermediates over Zk-$Fe_{0.1}$-ClNC (a) and Fe-N_4-C (b).

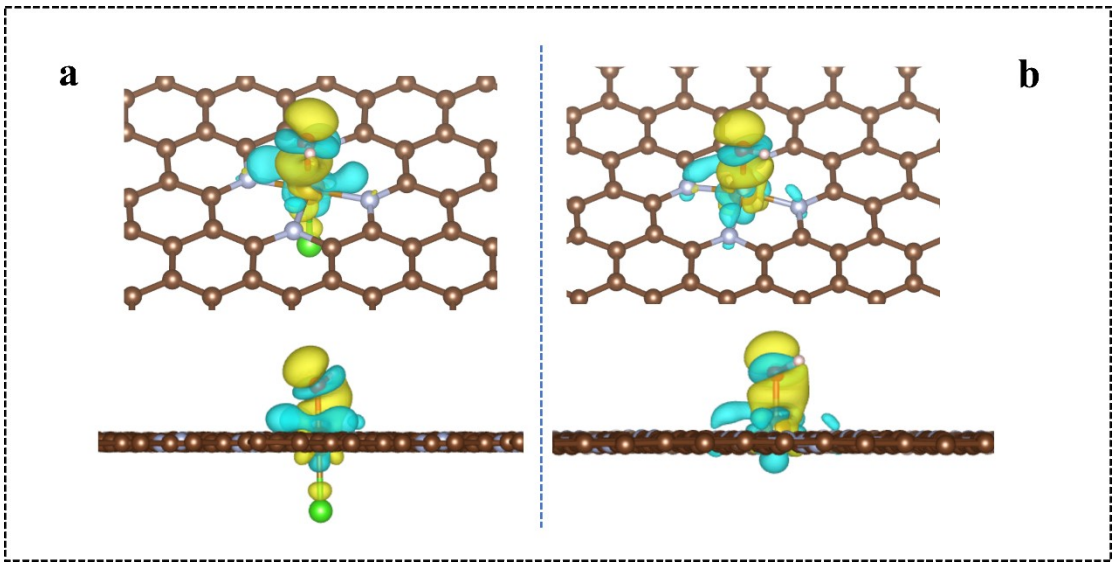

Figure S23. Analysis of charge density difference of *OH on the surfaces of Zk-$Fe_{0.1}$-ClNC and Fe-N_4-C

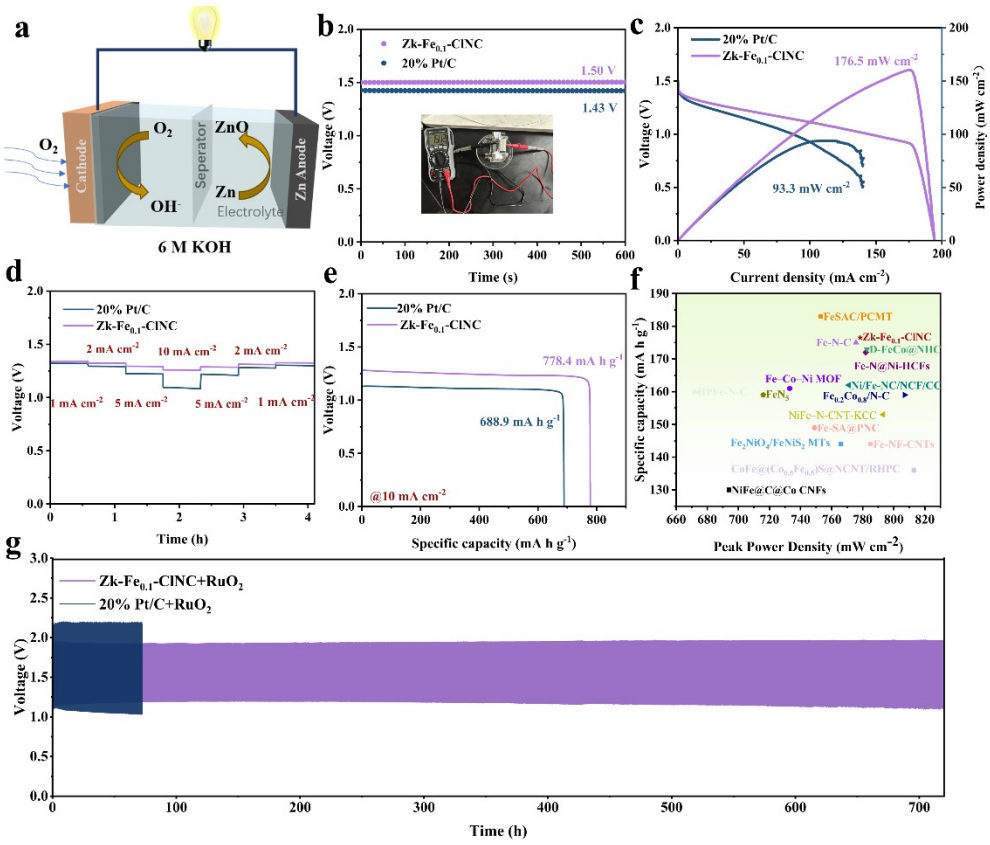

Figure S24. (a) Schematic diagram of a zinc-air battery, (b) open-circuit voltage, (c) discharge polarization curves and corresponding discharge power densities, (d) curves at different discharge currents, (e) specific capacity curves at a current concentration of 10 mA cm^{-2}, and (f) plots of power densities and specific capacities of zinc-air batteries compared with those of zinc-air batteries prepared with ORR catalysts in the recent article and (g) Charge-discharge cycling profiles of Zk-$Fe_{0.1}$-ClNC and 20% Pt/C-based zinc-air batteries at a current density of 5 mA cm^{-2}.

3.2 Supplemental Tables

Table.S1 BET specific surface area data of Zk-Fe_0-ClNC, Zk-$Fe_{0.1}$-ClNC and Z-$Fe_{0.1}$-NC.

Catalysts	BET Surface Area（m^2/g）	Pore Volume（cm^3/g）	Pore Size（nm）
Zk-Fe_0-ClNC	959.89	0.59	4.06
Zk-$Fe_{0.1}$-ClNC	1765.30	1.01	5.35
Z-$Fe_{0.1}$-NC	801.40	0.44	4.91

Table.S2 Contents of each element in Zk-Fe_0-ClNC, Zk-$Fe_{0.1}$-ClNC and Z-$Fe_{0.1}$-NC samples.

Catalysts	C (at. %)	N (at. %)	O (at. %)	Fe (at. %)	Cl (at. %)
Zk-Fe_0-ClNC	86.51	7.18	5.96	/	0.35
Zk-$Fe_{0.1}$-ClNC	83.80	6.54	7.89	0.84	0.37
Z-$Fe_{0.1}$-NC	79.97	9.40	10.29	0.34	/

Table.S3 Proportion of nitrogen content in Zk-Fe_0-ClNC, Zk-$Fe_{0.1}$-ClNC, and Z-$Fe_{0.1}$-NC samples.

Catalysts	Pyridinic-N (at. %)	Fe-N (at. %)	Pyrrolic-N (at. %)	Graphite-N (at. %)	Oxidized-N (at. %)
Zk-Fe_0-ClNC	0.34	/	0.25	0.21	0.2
Zk-$Fe_{0.1}$-ClNC	0.3	0.13	0.1	0.31	0.16
Z-$Fe_{0.1}$-NC	0.37	0.08	0.26	0.12	0.17

Table S4. EXAFS fitting parameters at the Fe K-edge for various samples.

Sample	Shell	N^a	R(Å)^b	σ^2(Å^2)^c	ΔE_0 (eV)^d	R factor
Fe foil	Fe-Fe	8 (set)	2.462±0.003	0.0051±0.0003	6.9±2.4	0.0012
	Fe-Fe	6 (set)	2.858±0.005			
Zk-$Fe_{0.1}$-ClNC	Fe-N	3.6±0.4	2.034±0.012	0.0087±0.0019	4.4±0.5	0.0017
	Fe-Cl	0.9±0.1	2.019±0.018			

$^a N$: coordination numbers; $^b R$: bond distance; $^c \sigma^2$: Debye-Waller factors; $^d \Delta E_0$: the inner potential correction. R factor: goodness of fit.

Table S5. An ORR activity comparison between recently reported electrocatalysts and our catalyst in alkaline conditions.

Catalysts	Loading (mg cm^{-2})	$E_{1/2}$ (V)	Reference
Zk-$Fe_{0.1}$-ClNC	**0.204**	**0.921**	**This work**
Sn SA/OCNTs	-	0.912	[1]
FeN_4-FeNCP@MCF	0.3	0.894	[2]
CR-Co/ClNC	-	0.93	[3]
VP/CNs	0.2	0.86	[4]
Fe_H-N-C	-	0.91	[5]
Fe-N_4/CNCl	0.764	0.917	[6]
CoTAACl@GR	0.46	0.818	[7]
H-3DOM-Co/ONC	0.2	0.84	[8]
T-Fe SAC	0.2	0.91	[9]
FeSA/N,S-PHLC	0.866	0.91	[10]
NCF	0.2	0.85	[11]
CeNC-40	0.63	0.90	[12]

Table S6. The performance of aqueous Zn-air batteries assembled with different oxygen electrocatalysts.

Name	Specific capacity (mA h g^{-1})	Peak Power Density (mW cm^{-2})	Reference
Zk-$Fe_{0.1}$-ClNC	**778.4**	**176.5**	**This work**
Fe-NF-CNTs	785	144	[13]
HPFe-N-C	672	160	[14]
Ni/Fe-NC/NCF/CC	771	162	[15]
Fe-N@Ni-HCFs	782	172	[16]
NiFe@C@Co CNFs	694	130	[17]
D-$_{Fe}$Co@NHC	782.7	173	[18]
FeSAC/PCMT	753	183	[19]
Fe_2NiO_4/$FeNiS_2$ MTs	766	144	[20]
Fe-N-C	775.7	175	[21]
CoFe@($Co_{0.5}Fe_{0.5}$)S@NCNT/RHPC	813	136	[22]
FeN_5	716	159	[23]
Fe–Co–Ni MOF	733	161	[24]
$Fe_{0.2}Co_{0.8}$/N-C	807	159	[25]
Fe/Cu-N-C	805	183	[26]
NiFe–N-CNT-KCC	793	153	[27]
Fe-SA@PNC	749	149	[28]

References

[1] X. Shao, R. Gan, Y. Rao, T.T.T. Nga, M. Liang, C.-L. Dong, C. Ma, J.Y. Lee, H. Li, H. Lee, ACS Nano 18 (2024) 14742–14753.

[2] Z. Wang, Z. Lu, Q. Ye, Z. Yang, R. Xu, K. Kong, Y. Zhang, T. Yan, Y. Liu, Z. Pan, Y. Huang, X. Lu, Advanced Functional Materials 34 (2024) 2315150.

[3] M. Liu, J. Zhang, H. Su, Y. Jiang, W. Zhou, C. Yang, S. Bo, J. Pan, Q. Liu, Nat Commun 15 (2024) 1675.

[4] H. Xia, R. Pang, X. Dong, Q. Liu, J. Chen, E. Wang, J. Li, J. Am. Chem. Soc. 145 (2023) 25695–25704.

[5] H. Tian, A. Song, P. Zhang, K. Sun, J. Wang, B. Sun, Q. Fan, G. Shao, C. Chen, H. Liu, Y. Li, G. Wang, Advanced Materials 35 (2023) 2210714.

[6] S. Wei, R. Yang, Z. Wang, J. Zhang, X. Bu, Advanced Materials 36 (2024) 2404692.

[7] B. Huang, X. Tang, Y. Hong, L. Li, T. Hu, K. Yuan, Y. Chen, Angewandte Chemie 135 (2023) e202306667.

[8] W. Yao, A. Hu, J. Ding, N. Wang, Z. Qin, X. Yang, K. Shen, L. Chen, Y. Li, Advanced Materials 35 (2023) 2301894.

[9] Y. Zhu, Y. Jiang, H. Li, D. Zhang, L. Tao, X. Fu, M. Liu, S. Wang, Angewandte Chemie 136 (2024) e202319370.

[10] M. Yuan, Y. Liu, Y. Du, Z. Xiao, H. Li, K. Liu, L. Wang, Adv Funct Materials 34 (2024) 2401484.

[11] L. Zhang, T. Gu, K. Lu, L. Zhou, D.-S. Li, R. Wang, Advanced Functional Materials 31 (2021) 2103187.

[12] Y. Zhao, H. Wang, J. Li, Y. Fang, Y. Kang, T. Zhao, C. Zhao, Advanced Functional Materials 33 (2023) 2305268.

[13] Y. Liu, X. Liu, C. Zhang, Y. Chen, Z. Wang, G. Wei, J. Zhang, T. Yang, F. Zhang, S. Gao, Journal of Alloys and Compounds 941 (2023) 168922.

[14] H. Xu, D. Wang, P. Yang, L. Du, X. Lu, R. Li, L. Liu, J. Zhang, M. An, Applied Catalysis B: Environmental 305 (2022) 121040.

[15] C. Lai, M. Li, Y. Shen, M. Zhou, W. Wang, K. Jiang, H. Li, K. Wang, Energy & Environ Materials 7 (2024) e12541.

[16] Y. Tian, Z. Wu, M. Li, Q. Sun, H. Chen, D. Yuan, D. Deng, B. Johannessen, Y. Wang, Y. Zhong, L. Xu, J. Lu, S. Zhang, Adv Funct Materials 32 (2022) 2209273.

[17] X. Chen, J. Pu, X. Hu, Y. Yao, Y. Dou, J. Jiang, W. Zhang, Small 18 (2022) 2200578.

[18] S. Wu, X. Liu, H. Mao, T. Cui, B. Li, G. Zhou, L. Wang, Applied Catalysis B: Environmental 330 (2023) 122634.

[19] H. Zhang, Y. Meng, H. Zhong, L. Zhang, S. Ding, L. Fang, T. Li, Y. Mei, P. Hou, C. Liu, S.P. Beckman, Y. Lin, H. Cheng, J. Li, Carbon Energy 5 (2023) e289.

[20] X. Li, D.C. Nguyen, K. Dong, S. Prabhakaran, D.T. Tran, D.H. Kim, N.H. Kim, J.H. Le, Chemical Engineering Journal 489 (2024) 151210.

[21] X. Lu, H. Xu, P. Yang, L. Xiao, Y. Li, J. Ma, R. Li, L. Liu, A. Liu, V. Kondratiev, O. Levin, J. Zhang, M. An, Applied Catalysis B: Environmental 313 (2022) 121454.

[22] J. Yang, J. Shi, Y. Wu, H. Liu, Z. Liu, Q. You, X. Li, L. Cong, D. Liu, F. Liu, Y. Jiang,

N. Lin, W. Zhang, H. Lin, J. Mater. Chem. A 12 (2024) 11907–11919.
[23] M. Wang, L. Wang, Q. Li, D. Wang, L. Yang, Y. Han, Y. Ren, G. Tian, X. Zheng, M. Ji, C. Zhu, L. Peng, G.I.N. Waterhouse, Small 19 (2023) 2300373.
[24] F. Shahbazi Farahani, M.S. Rahmanifar, A. Noori, M.F. El-Kady, N. Hassani, M. Neek-Amal, R.B. Kaner, M.F. Mousavi, J. Am. Chem. Soc. 144 (2022) 3411–3428.
[25] H. Huang, Q. Liang, H. Guo, Z. Wang, G. Yan, F. Wu, J. Wang, Small 20 (2024) 2310318.
[26] M. Bu, Y. Liu, S. Liao, W. Liu, Z. Yang, J. Jiang, X. Gao, Y. Yang, H. Liu, Carbon 214 (2023) 118365.
[27] M.B. Poudel, S. Vijayapradeep, K. Sekar, J.S. Kim, D.J. Yoo, J. Mater. Chem. A 12 (2024) 10185–10195.
[28] M. Shen, J. Qi, K. Gao, C. Duan, J. Liu, Q. Liu, H. Yang, Y. Ni, Chemical Engineering Journal 464 (2023) 142719.